Eur. Phys. J. Special Topics **223**, 2253–2267 (2014)

DOI: 10.1140/epjst/e2014-02262-3

THE EUROPEAN PHYSICAL JOURNAL SPECIAL TOPICS

Review

Recent advances in the simulation of particle-laden flows

J. Harting[1,2,a], S. Frijters[1], M. Ramaioli[3], M. Robinson[4], D.E. Wolf[5], and S. Luding[6]

[1] Department of Applied Physics, Eindhoven University of Technology, PO Box 513, 5600MB Eindhoven, The Netherlands
[2] Faculty of Science and Technology, Mesa+ Institute, University of Twente, PO Box 217, 7500AE Enschede, The Netherlands
[3] Environmental Hydraulics Laboratory, École Polytechnique Fédérale de Lausanne, 1015 Lausanne, Switzerland
[4] Mathematical Institute, University of Oxford, Andrew Wiles Building, Radcliffe Observatory Quarter, Woodstock Road, Oxford OX2 6GG, UK
[5] Department of Physics, University of Duisburg-Essen, Lotharstr.1, 47057 Duisburg, Germany
[6] MSM, MESA+, CTW, Department of Engineering Technology, University of Twente, PO Box 217, 7500AE Enschede, The Netherlands

Received 12 June 2014 / Received in final form 18 August 2014
Published online 24 October 2014

Abstract. A substantial number of algorithms exists for the simulation of moving particles suspended in fluids. However, finding the best method to address a particular physical problem is often highly non-trivial and depends on the properties of the particles and the involved fluid(s) together. In this report, we provide a short overview on a number of existing simulation methods and provide two state of the art examples in more detail. In both cases, the particles are described using a Discrete Element Method (DEM). The DEM solver is usually coupled to a fluid-solver, which can be classified as grid-based or mesh-free (one example for each is given). Fluid solvers feature different resolutions relative to the particle size and separation. First, a multicomponent lattice Boltzmann algorithm (mesh-based and with rather fine resolution) is presented to study the behavior of particle stabilized fluid interfaces and second, a Smoothed Particle Hydrodynamics implementation (mesh-free, meso-scale resolution, similar to the particle size) is introduced to highlight a new player in the field, which is expected to be particularly suited for flows including free surfaces.

1 Introduction

Particles suspended in fluids are common in our daily life. Examples include human blood (which is to good approximation made of particulate red blood cells suspended in plasma) [1–5], or tooth paste and wall paint, which are mixtures of finely ground

[a] e-mail: j.harting@tue.nl

solid ingredients in fluids, as well as e.g. geophysical debris flow [6]. Extreme examples are the sand on a beach or in a desert, when blown away by the wind [7,8], or industrial gas phase synthesis of nanoparticles [9]. Also every-day food-powders as we use them in our kitchen, related to the dispersion of instant-drinks [10], are challenging examples of particle-fluid systems.

Long-range fluid-mediated hydrodynamic interactions often dictate the behavior of particle-fluid mixtures. The majority of analytical results for the particle scale behavior of suspensions has been obtained in the regime of vanishing Reynolds numbers (viscous flow) since an analytical treatment of the full Navier-Stokes equations is generally difficult or even impossible. Computer simulation methods are indispensable for many-particle systems, for the inclusion of inertia effects (Reynolds numbers > 1) and Brownian motion (Peclet number of order 1). These systems often contain various important time scales that can differ by many orders of magnitude, but nevertheless have to be resolved by the simulation, leading to multiscale problems that can only be solved by a large numerical effort.

Many simulation methods have been developed to simulate particle-fluid mixtures, including the early works by pioneers as Tsuji and Herrmann [7,11–13]. Examples for more recent reviews on research on multi-phase and particle fluid flow models, including their experimental validation and approaches at different scales of resolution are provided in Refs. [6,8,14–22] and references therein. All of them have their inherent strengths but also some disadvantages and can generally be divided into two separate classes: The methods in the first category restrict the treatment of the fluid to approximations of the hydrodynamic interactions between suspended particles only, while the methods in the second category try to tackle all degrees of freedom of the involved fluids by approximating the Navier-Stokes equations.

The simplest approach is Brownian Dynamics which does not contain long-ranged hydrodynamic interactions among particles at all [23]. Brownian Dynamics with full hydrodynamic interactions utilizes a mobility matrix which is based on tensor approximations which are exact in the limit of zero Reynolds number and zero particle volume fraction [24,25]. However, the computational effort scales with the cube of the particle number due to the inversion of matrices. Pair-Drag simulations have been proposed by Silbert et al. [26], and include hydrodynamic interactions in an approximative way. They have focused on suspensions with high densities (up to 50%) of uncharged spherical colloidal particles. Stokesian Dynamics has been presented by Bossis and Brady in the 80s and applied subsequently e.g. in [27–30]. However, as the previous examples, this method is limited to Reynolds numbers close to zero. The inclusion of long-range hydrodynamic interactions causes the computational effort to become very high for dynamical simulations with many particles and makes an efficient parallelization difficult. The method is still widely used due to its physical motivation and its robustness. Boundary-element methods are more flexible than Stokesian dynamics and can also be used to simulate non-spherical or deformable particles, but the computational effort is even higher [31].

As stated above, these methods represent the hydrodynamic interactions between suspended particles in an approximative way. If the level of approximation is not well chosen, it might lead to unphysical artifacts, as was shown for example by Knudsen et al. [32], who studied a system where electrostatic repulsion and hydrodynamic interactions between particles were both important. They found that even for dilute systems some existing models overestimate the effect of hydrodynamic damping leading effectively to an attraction of like-charged particles.

Furthermore, all the methods listed above assume that hydrodynamic interactions are fully developed and that the dynamics of the fluid and of the solved particles can be treated separately. In reality, this is not the case. Hydrodynamic interactions are time dependent due to local stresses at the fluid-particle interfaces. A number of more

recent methods attempt to describe the time dependent long-range hydrodynamics properly with the computational effort scaling linearly with the number of particles. These include recent mesoscopic methods like Dissipative Particle Dynamics [33], the lattice Boltzmann method [34,35], Stochastic Rotation Dynamics/Multi Particle Collision Dynamics [36–40], or Smoothed Particle Hydrodynamics [10,18,41]. However, for small Reynolds numbers, the computational gain of these methods is lost due to the additional effort needed to describe the motion of the fluid.

Finite element or finite difference methods need a proper meshing of the computational domain which is not trivial for complicated boundary conditions as in the case of dense suspensions. Therefore, many authors only simulated a limited number of static configurations rather than the full dynamics of the system. Advances in remeshing techniques as well as more powerful computers have allowed to overcome these problems. Also, in order to avoid remeshing at all, uniform grids can often be used [42–46]. Another recent class of simulation methods involves moving grids see Refs. [19,21,22] and references therein.

If the particles are very massive and the density of the fluid is very low, a full hydrodynamic treatment of the solvent is not needed anymore. Then, a coarse-grained description of the fluid where the fluid is resolved on a length scale larger than the particles might be sufficient. Much larger systems can be treated this way, but the coarse-graining is justified only in certain situations. An example is the pneumatic transport of a powder in a pipe which is a common process in many industrial applications [12,47–49].

In the remainder of this paper we give examples, where simplified approaches to treat hydrodynamic interactions between suspended particles are supposed to fail. First, we review recent work on the interplay of particle laden flows with fluid interfaces. The simulation method of choice here is based on a Discrete Element Method (DEM) and a multiphase lattice Boltzmann algorithm, where the fluid is resolved considerably better than the particles. Then, we introduce an application of a relatively new player in the field, i.e. a combined DEM and Smoothed Particle Hydrodynamics approach, which has its strength in the simulation of systems containing free fluid interfaces, while leaving the fluid "meso-resolved", on a scale slightly larger than the particle diameter.

2 Particles in multicomponent fluid flows

2.1 The lattice Boltzmann – Discrete Element Method

The use of particles as an alternative to surfactants for the stabilization of emulsions is very attractive, such as in the food, cosmetics, and medical industries, where they are used to stabilize barbecue sauces and sun cremes, or to produce sophisticated ways to deliver drugs at the right position in the human body. The microscopic processes leading to the commercial interest can be understood by assuming an oil–water mixture. Without any additives, the phases would seperate and the oil would float on top of the water. Adding small particles, however, causes these particles to diffuse to the interface, which is then stabilized due to a reduced surface energy. If, for example, individual droplets of one phase are covered by particles, such systems are also referred to as "Pickering emulsions" [50,51]. Particularly interesting properties of such emulsions are the blocking of Ostwald ripening and their complex rheology due to irreversible particle adsorption at interfaces.

Computer simulations are a promising route to understanding the dynamics of particle stabilized emulsions. However, the shortcomings of traditional simulation methods quickly become obvious: a suitable algorithm is not only required to deal

with simple fluid dynamics but has to be able to simulate several fluid species while also considering the motion of the particles and the fluid-particle interactions. Some recent approaches trying to solve these problems utilize the lattice Boltzmann method (LBM) for the description of the solvents [52]. The LBM is an alternative to conventional Navier-Stokes solvers and is well established in the literature. It is attractive for the current application since a number of multiphase and multicomponent models exist which are comparably straightforward to implement [53–56]. In addition, the method has been combined with a discrete elements method (DEM) to simulate arbitrarily shaped particles in flow and is commonly used to study the behavior of particle-laden single phase flows [34,35,57].

A few groups combined multiphase lattice Boltzmann solvers with the known algorithms for suspended particles [58–61]. Here, an approach based on the multicomponent lattice Boltzmann model of Shan and Chen is used which allows the simulation of multiple fluid components with surface tension [53,60–62]. The model generally allows arbitrary movements and rotations of arbitrarily shaped hard shell particles. Further, it allows an arbitrary choice of the particle wettability – one of the most important parameters for the dynamics of multiphase suspensions [63,64].

In the LBM, the fluid is treated as a cluster of pseudo-particles that move on a lattice under the action of external forces. A distribution function f_i is associated to each pseudo-particle, which denotes the probability to find the particle at a position $\mathbf{r}$ and with a velocity in direction $\mathbf{e}_i$. Position and velocity spaces are both discretised, where Δx defines the grid spacing, and $\mathbf{e}_i$ are the discretised velocity directions. Here, we use a 3D lattice defined by 19 discrete velocities (D3Q19). Together with the discrete time step Δt, the time evolution of f_i is governed by the so-called lattice Boltzmann equation,

$$f_i(\mathbf{r} + \mathbf{e}_i \Delta t, t + \Delta t) - f_i(\mathbf{r}, t) = \Omega_i. \tag{1}$$

The left-hand side of Eq. (1) denotes advection, while the right hand-side is given by the collision operator Ω_i specifying the collision rate between the fluid pseudo-particles. From now on, we set Δx, Δt and the unit mass to unity for convenience. A simple approximation is the Bhatnagar-Gross-Krook (BGK) operator, $\Omega_i = -(f_i - f_i^{\mathrm{eq}})/\tau$, which describes the relaxation of f_i towards its local equilibrium, f_i^{eq}, on a time scale τ. The relaxation time defines the macroscopic dynamical viscosity η via $\eta = \rho c_{\mathrm{s}}^2 \frac{\Delta x^2}{\Delta t} \left(\tau - \frac{1}{2}\right)$, where $c_{\mathrm{s}} = 1/\sqrt{3}$ is the lattice speed of sound. The equilibrium distribution is given by a truncated and discretized Maxwell–Boltzmann distribution [52].

In the Shan-Chen multi-component model [53], each species σ of k miscible or immiscible fluids is described by a set of distribution functions $f_{\sigma,i}$. As a consequence, k lattice Boltzmann equations with relaxation times τ_σ have to be iterated. The interaction between the fluid species is mediated via a local force density,

$$\mathbf{F}_\sigma(\mathbf{r}, t) = -\Psi_\sigma(\mathbf{r}, t) \sum_{\sigma'} g_{\sigma\sigma'} \sum_{\mathbf{r}'} \Psi_{\sigma'}(\mathbf{r}', t)(\mathbf{r}' - \mathbf{r}), \tag{2}$$

which is then added to the right hand side of Eq. (1). Here, the contributions of all species σ' are taken into account, and the force density acting on species σ is obtained. The sum runs over all neighbouring sites $\mathbf{r}'$ of site $\mathbf{r}$. $g_{\sigma\sigma'}$ is a coupling constant defining the interaction strength between species σ and σ'. It is related to the surface tension between both species. The pseudopotential Ψ_σ is a function of the density ρ_σ, in our case $\Psi_\sigma = 1 - \exp(-\rho_\sigma)$. It defines the equation of state of the multicomponent system. The Shan-Chen model belongs to the class of front capturing methods. It is suitable to track interfaces for which the topology evolves in time, for example, the deformation or even breakup of a droplet in a shear flow – as in the current section.

If there is no clear scale separation between immersed particles and the lateral interface extension, it may be necessary to model the particles explicitly. Here, we consider an ensemble of particles with well-defined wetting behaviour. The particles themselves may have a complex shape and can be supplied with a constitutive model (of which the simplest is a rigid particle model as we use it here). There are several approaches to simulate a system of two immiscible fluids and particles. One example which has recently been applied by several groups is to couple Molecular Dynamics (MD) or the Discrete Element Method (DEM) to the LBM [58–62,65,66]. The advantage of this combination is the possibility to resolve the arbitrarily shaped particles as well as both fluids in such a way that all relevant hydrodynamical properties are included.

The suspended particles are discretised on the lattice of the fluid solver. Following the approach originally proposed by Ladd [34], populations propagating from fluid to particle sites are bounced back in the direction they came from. Then they receive additional momentum due to the motion of the particles. In order to satisfy the local conservation laws, linear and angular momentum contributions are assigned to the corresponding particles as well. These in turn are used to update the particle positions and orientations. In the multi-component algorithm used here, the outermost sites covered by a particle are filled with a virtual fluid corresponding to a suitable average of the surrounding unoccupied sites. This approach provides accurate dynamics of the two-component fluid near the particle surface. The wetting properties of the particle surface can be controlled by shifting the local density difference of both fluid species which leads to a well-defined contact angle θ_p on the particle surface [60–62].

All simulation algorithms for suspensions combining a DEM for the suspended particles with a discretized solver of the underlying Navier-Stokes dynamics suffer from the finite resolution of the fluid solver: when two particles approach each other, there is always a distance below which the fluid solver is not able to resolve the hydrodynamic interactions anymore. This generally causes a depletion interaction between particles which one can overcome by adding a lubrication correction to the DEM part of the algorithm which acts on very small distances [60,62,67,68].

2.2 Dimensionless numbers

Here, we present as an example an application where the particle-laden flow needs to be treated by an algorithm which is able to handle moderate Reynolds numbers as well as multiple fluid phases. This section represents a summary of some results given in more detail in a recent article by Frijters et al. [61] and the reader is referred to this article for details of the implementation and simulation parameters. A fraction χ of the interface of a droplet is covered with particles while a shear flow is imposed on a second fluid surrounding the droplet. This shear flow causes the droplet to deform – a process which is common in the transport of particle stabilized emulsions or their production process. The deformation of the droplet can be quantified using the dimensionless deformation parameter

$$D \equiv \frac{L - B}{L + B} \tag{3}$$

introduced by Taylor [69,70], where L is the length and B is the breadth of the droplet. A deformed droplet has lost its spherical shape and thus gains a preferred alignment. In the limit of small deformations, Taylor predicts a linear dependence of the deformation of a droplet on the capillary number (see Eq. (4)), with a particularly simple form for equiviscous fluids, i.e. $D = 35/32\mathrm{Ca}$. Due to the finite system size, we define the capillary and Reynolds numbers in terms of an effective shear rate $\dot{\gamma}^{\mathrm{eff}}$,

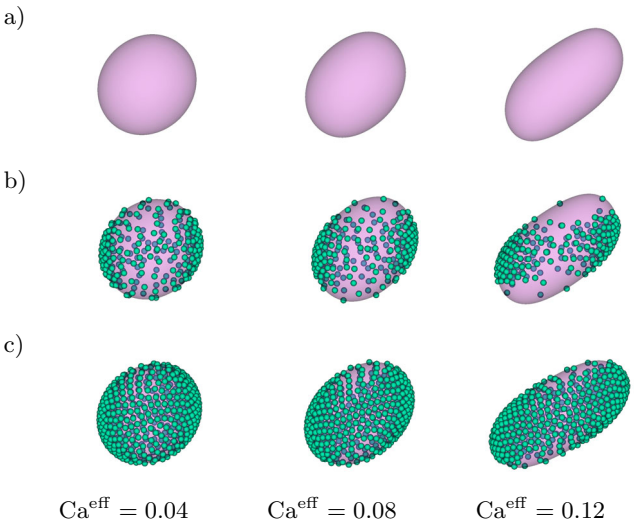

Fig. 1. Side-view examples of deformed droplets, for various particle coverage fractions: a) $\chi = 0.00$, b) $\chi = 0.27$ and c) $\chi = 0.55$. Although increasing χ from 0 to 0.27 does not strongly change the deformation of the droplet, the particles prefer to stay in the middle of the channel where the shear flow is weakest. The particles also exhibit tank-treading-like behaviour: they move around the interface following the shear flow (reprinted from [61] – reproduced by permission of The Royal Society of Chemistry).

which is measured at the interface of the droplet during the simulation instead of the shear rate $\dot{\gamma}$ applied via the moving boundaries:

$$\mathrm{Ca}^{\mathrm{eff}} \equiv \frac{\mu_m \dot{\gamma}^{\mathrm{eff}} R_d}{\sigma}, \qquad \mathrm{Re}^{\mathrm{eff}} \equiv \frac{\rho_m \dot{\gamma}^{\mathrm{eff}} R_d^2}{\mu_m}, \tag{4}$$

where μ_m is the dynamic viscosity of the medium, R_d is the radius of the initial – undeformed, hence spherical – droplet and σ is the surface tension. We also define the ratio of the droplet and medium viscosity $\lambda \equiv \mu_d/\mu_m = 1$ in all presented data. The effective Reynolds number is varied between approximately $0.6 < \mathrm{Re}^{\mathrm{eff}} < 25$.

2.3 Distribution of nanoparticles

To understand the effect of nanoparticles on the deformation properties of the droplet, we first discuss how they position themselves at and move over the droplet interface as the droplet is sheared. The fluid–fluid interaction strength is held fixed at $g_{br} = 0.10$. The particles have a radius of $r_p = 5.0$ and are neutrally wetting ($\theta_p = 90°$). We choose their mass to be $m_p = 524$, i.e. identical to the fluid mass density. The introduction of finite-sized particles introduces a lower bound on how small the simulation volume can be to accomodate enough particles on the interface and to avoid finite-size effects. For this reason, the simulation volume is chosen to be $n_x = n_y = 256$, $n_z = 512$, with an initial droplet radius of $R_d^{\mathrm{init}} = 0.3 \cdot n_x = 76.8$, still keeping it as small as possible to avoid excessive calculation time. The number of particles is varied as $n_p = 0$, 128, 256, 320, 384, 446 and 512, which results in a surface coverage fraction of $\chi = 0$ up to $\chi = 0.55$. The capillary number is changed by changing the shear rate. Some examples of the deformations thus realised are shown in Fig. 1, for $\mathrm{Ca}^{\mathrm{eff}} = 0.04$, 0.08, 0.12 and $\chi = 0.0$ (a), $\chi = 0.27$ (b) and $\chi = 0.55$ (c).

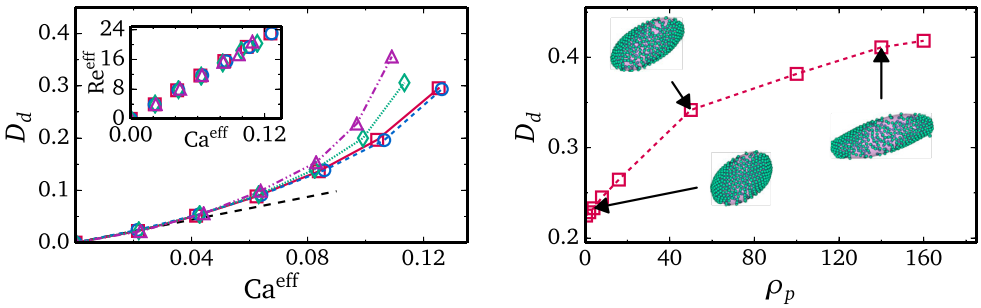

Fig. 2. Left: the main plot shows the deformation parameter D as a function of the effective capillary number $\mathrm{Ca}^{\mathrm{eff}}$ for various degrees of droplet interface particle coverage fraction χ: $\chi = 0$ (red squares), $\chi = 0.27$ (blue circles), $\chi = 0.41$ (green diamonds), and $\chi = 0.55$ (purple triangles). The effect of adsorped particles is very weak for low χ, becomes noticeable at $\chi > 0.4$. Taylor's law is reproduced for small Ca (dashed line). The inset depicts that the Reynolds number scales linearly with the capillary number. Right: the deformation parameter D is shown as a function of the rescaled mass of the particles $m_p^* = m_p/m_p^0$, where $m_p^0 = 524$ is defined by setting the density of the particle to 1. The particles have a radius $r_p = 5.0$, their coverage fraction is $\chi = 0.55$ and the capillary number is $\mathrm{Ca}^{\mathrm{eff}} = 0.1$. Snapshots of the droplets are included, showcasing the deformations of the droplet. The inertia of the heavier particles causes additional deformation as they drag the droplet interface in the direction of the shear flow (reprinted from [61] – reproduced by permission of The Royal Society of Chemistry).

When a droplet is sheared, its interfacial area increases due to the resulting deformation, and more space is available for the particles to move freely over the interface (cf. Fig. 1). However, even for high particle coverages and shear rates, detaching particles from the interface remains practically impossible. The particles are swept over the interface with increasing velocity as they move away from the center plane of the system and up the shear gradient. If the particles would not be affected by the shear flow, they would prefer to occupy interface with high local curvature as can be explained by a geometrical argument: the interface removed by a spherical particle at a curved interface is larger than the circular area removed from a flat interface, and this effect gets stronger as curvature increases. This explains why in this dynamic equilibrium, most particles can be found at the tips of the droplet. This can be observed in Fig. 1b at high capillary number.

Even though the overall structure of the particles on the droplet interface remains stable over time, individual particles move over the interface, performing a quasi-periodic motion. However, this effect is qualitatively different from the tank-treading behaviour observed in, for example, vesicles [71]. While tank-treading vesicles are characterized by a constant frequency of rotation for all points on their membrane, this is not the case for the particle covered droplets: The rotational frequency is not constant for all particles, instead showing a dependence on the position of the particle, normal to the shear plane. The deformation is highest at the center of the droplet surface, giving particles greater options for mobility that are also better-aligned with the shear flow, leading to increased particle velocities.

2.4 Droplet deformation and inclination

The linear dependence of the deformation parameter D on the effective capillary number introduced above is recovered in our simulations for low capillary number and low particle coverage (cf. Fig. 2, left). When the coverage fraction grows beyond

$\chi > 0.40$ the deformations in this regime increase with increasing χ and constant capillary number.

Combining Eq. (4) gives a relation between the capillary and Reynolds number:

$$\mathrm{Re}^{\mathrm{eff}} = \sigma \left(\frac{\rho_m R_d}{\mu_m^2} \right) \mathrm{Ca}^{\mathrm{eff}}. \tag{5}$$

As we change the capillary number explicitly by changing the shear rate, the Reynolds number is proportional to the capillary number for a fixed value of the surface tension. Inertial effects increase the deformation, thus the deformations at high capillary number are higher than predicted by the linear relation of Taylor. Furthermore, since the nanoparticles do not affect the surface tension, all curves of the Reynolds number versus capillary number have the same slope (cf. inset of Fig. 2(left) and Eq. (5)). This implies that the increased deformation in the case of added nanoparticles is not caused by changes in inertia of the fluids. On the other hand, the inertia of the particles themselves plays a decisive role here. We have investigated the dependence of the droplet deformation on the size and mass of the particles. Particle radii have been varied between $4.0 \leq r_p \leq 10.0$ and at $\mathrm{Ca}^{\mathrm{eff}} = 0.1$ this has led to only a small change in D. Yet, changing the mass of the particles directly has a substantial effect. We have varied the mass of the particles over two orders of magnitude, as shown in Fig. 2(right). $\chi = 0.55$ and $\mathrm{Ca}^{\mathrm{eff}} = 0.1$ are kept constant and we have rescaled the mass scale with the reference mass: $m_p^* = m_p/524$. The particles are accelerated as long as they are on the part of the droplet interface that experiences a shear flow at least partially parallel to the particle movement. Eventually, particles have to "round the corner" and are forced to move perpendicular to or even antiparallel to the shear flow. The increased inertia of heavier particles makes it more difficult to change the movement of these particles, leading to a situation where the droplet interface is in fact initially dragged farther away in the direction of the shear flow instead. This process is balanced by the surface tension as the surface area increases. This then explains the increase of deformation with increasing particle mass. As our deformation is increased substantially, the system size limits the deformation we can induce. Therefore, the values presented here are underpredictions of the actual effect of increased mass at high deformations, and might indeed hide a breakup event.

3 Meso-resolved Particle-Fluid Method

This section is based on Refs. [10,18,41], where a meso-scale solver for particles dispersed in a fluid was presented. Both phases are tackled by particle-based methods – which facilitates their coupling – where the fluid has a resolution somewhat larger than the discrete phase.

The SPH-DEM formulation is applied to several test cases for verification and validation, before it is used to predict a dispersion experiment with free-surfaces involved, which shows the quality of this particle-based method. The agreement between model and simulation is very good, however, the feature of lift-off of the packed bed is not reproduced yet. This can have various reasons, since some features like the interstitial gas, the surface tension and the polydispersity of the grain-packing, are not implemented yet and are subject of ongoing research.

3.1 The Smoothed Particle Hydrodynamics – Discrete Element Method

We present a discrete particle method (DPM) based on the coupling of Smoothed Particle Hydrodynamics (SPH) for the fluid phase and the discrete element method

(DEM) for the solid particles. This resuls in a purely particle-based simulation method and enjoys the intrinsic flexibility as a primary advantage over existing grid-based DPMs. The model described in this section is well suited for applications involving a free surface, including (but not limited to) debris flows, avalanches, landslides, sediment transport or erosion in rivers and beaches, slurry transport in industrial processes (e.g. SAG mills) and liquid-powder dispersion and mixing in the food processing industry [41]. Here we briefly describe the governing SPH equations for the fluid phase, based on the locally averaged Navier-Stokes equations (LANSEs) [72]; for more details see Ref. [18].

First, we define a smooth porosity field by smoothing out the DEM particle's volumes according to the SPH interpolation kernel $W_{aj}(h) = W(r_a - r_j, h)$

$$\epsilon_a = 1 - \sum_j W_{aj}(h) V_j, \tag{6}$$

where V_j is the volume of DEM particle j. For readability, sums over SPH particles use the subscript b, while sums over surrounding DEM particles use the subscript j. To calculate the continuity and momentum equations in the LANSEs, we first define a superficial fluid density ρ equal to the intrinsic fluid density scaled by the local porosity $\rho = \epsilon \rho_f$. Substituting the superficial fluid density into the averaged continuity and momentum equations reduces them to the normal Navier-Stokes equations. Therefore, our approach is to use the weakly compressible SPH equations with variable h (resolution/smoothing length) terms [73–75] and adding fluid-particle drag terms (as specified below). The rate of change of the superficial density then becomes

$$\begin{aligned} \frac{D\rho_a}{Dt} &= \frac{1}{\Omega_a} \sum_b m_b \mathbf{u}_{ab} \cdot \nabla_a W_{ab}(h_a), \\ \Omega_a &= 1 - \frac{\partial h_a}{\partial \rho_a} \sum_b m_b \frac{\partial W_{ab}(h_a)}{\partial h_a}, \end{aligned} \tag{7}$$

where $\mathbf{u}_{ab} = \mathbf{u}_a - \mathbf{u}_b$ is the difference in velocity between SPH-particles a and b and Ω_a is a correction factor due to the variable h. Second, the acceleration of SPH-particle a is given by

$$\begin{aligned} \frac{d\mathbf{u}_a}{dt} = -\sum_b m_b \Bigg[&\left(\frac{P_a}{\Omega_a \rho_a^2} + \Pi_{ab} \right) \nabla_a W_{ab}(h_a) \\ &+ \left(\frac{P_b}{\Omega_b \rho_b^2} + \Pi_{ab} \right) \nabla_a W_{ab}(h_b) \Bigg] + \mathbf{f}_a / m_a, \end{aligned} \tag{8}$$

where $\mathbf{f}_a$ is the coupling force on the SPH particle a due to the DEM particles. The term Π_{ab} models the effect of the viscous stress tensor and is calculated here using the term proposed in Ref. [73]

$$\Pi_{ab} = -\alpha \frac{u_{\text{sig}} u_n}{2\overline{\rho}_{ab} |\mathbf{r}_{ab}|}, \tag{9}$$

where $\overline{\rho}_{ab}$ and $\mathbf{r}_{ab}$ are the average density and the distance between the centers of two SPH particles a and b, u_n is the normal component of the relative velocity, and $u_{\text{sig}} = c_s + u_n / |\mathbf{r}_{ab}|$ is a signal velocity at which information propagates between the particles. The (numerical) sound speed is given by c_s and α is a numerical pre-factor.

Third, the fluid pressure in Eq. (8) is calculated using the weakly compressible equation of state where the reference density ρ_0 is scaled by the local porosity to

ensure that the pressure is slowly varying with porosity as

$$P_a = B\left(\left(\frac{\rho_a}{\epsilon_a \rho_0}\right)^{\gamma} - 1\right), \tag{10}$$

where $B = 100\rho_0 u_m^2/\gamma$ is a scaling factor that is free a priori. It is set using a maximum velocity u_m, in order to ensure that density fluctuations (due to the weakly compressible SPH formulation) are below 1%. The smoothing length h_a varies according to the superficial density (and hence with the porosity) and is calculated by $h_a = 1.5(m_a/\rho_a)^{1/3}$.

Finally, the suspended particles are introduced as follows: Given a DEM particle i with position $\mathbf{r}_i$, the equation of motion is

$$m_i \frac{d^2\mathbf{r}_i}{dt^2} = \sum_j \mathbf{c}_{ij} + \mathbf{f}_i + m_i\mathbf{g}, \tag{11}$$

where m_i is the mass of particle i, $\mathbf{c}_{ij}$ is the contact force between particles i and j (acting from j to i) and $\mathbf{f}_i$ is the fluid-particle coupling force on particle i. For the simulations presented below, we have used the linear spring dashpot contact model

$$\mathbf{c}_{ij} = -(k\delta - \beta\dot{\delta})\mathbf{n}_{ij}, \tag{12}$$

where δ is the overlap between the two particles and $\mathbf{n}_{ij}$ is the unit normal vector pointing from j to i. The force on each solid particle by the fluid is [72]

$$\mathbf{f}_i = V_i(-\nabla P + \nabla \cdot \tau)_i + \mathbf{f}_d(\epsilon_i, \mathbf{u}_s), \tag{13}$$

where V_i is the volume of particle i. The first two terms model the effect of the resolved fluid forces (buoyancy and shear-stress) on the particle. The fluid pressure gradient and the divergence of the stress tensor are already calculated in Eq. (8) and are evaluated at each solid particle, using a Shepard corrected SPH interpolation [18].

The force $\mathbf{f}_d$ models the drag effects of the unresolved fluctuations in the fluid variables and is calculated from the local porosity ϵ_i and the superficial velocity $\mathbf{u}_s = \epsilon_i(\mathbf{u}_f - \mathbf{u}_i)$. These two values are calculated at each DEM particle position, again using a Shepard corrected SPH interpolation. For the results in this paper, we use both the simple Stokes drag force and a more general drag law proposed by Di Felice [76].

The coupling force on SPH particle a is determined by a weighted average of the fluid-particle coupling force on the surrounding DEM particles.

$$\mathbf{f}_a = -\frac{m_a}{\rho_a}\sum_j \frac{1}{S_j}\mathbf{f}_j W_{aj}(h_c), \tag{14}$$

where $\mathbf{f}_j$ is the coupling force calculated for each DEM particle using Eq. (13) and $S_j = \sum_b \frac{m_b}{\rho_b} W_{jb}(h_c)$ is a correction factor to guarantee equal and opposite forces between the two phases.

3.2 Verification case 1: Single Particle Sedimentation

The first test case models a single particle sedimenting (SPS) in a 3D fluid column under gravity [10]. The water column has a height of $H = 0.006\,\mathrm{m}$, and the bottom has a no-slip boundary, while the boundaries in the x and y directions are periodic

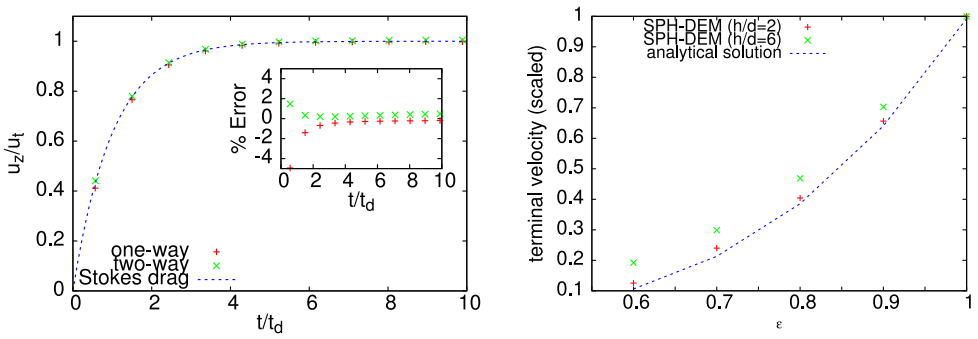

Fig. 3. Left: sedimentation velocity for a single particle in water falling from rest with both one-way and two-way coupling. The dashed line is the theoretical result integrating Stokes law. The y-axis shows the particle vertical velocity scaled by the expected terminal velocity $u_t = |\mathbf{u}_t|$ and the x-axis shows time scaled by the drag relaxation time t_d. The inset shows the percentage error between the SPH-DEM and the theoretically expected trajectory. Right: average terminal velocity (scaled by $|\mathbf{u}_t|$, the expected terminal velocity of a single DEM particle) of the Constant Porosity Block (CPB) in water for varying porosity and $h/d = 2$ and 6, compared to the analytical solution (dashed line).

with a width of $w = 0.004$ m. Gravity acts in the negative z direction, so that the single DEM particle, initialised at $z = 0.8H$, with diameter $d = 10^{-4}$ m and density $\rho_p = 2500$ kg/m^3 starts to fall at $t = 0$ s. Note that before the SPS starts, for the initial conditions of the simulation, the position of the DEM particle is fixed and the SPH fluid particles are allowed to reach their hydrostatic equilibrium positions, which are not necessarily the same as their input positions.

In Fig. 3(left) the evolution of a DEM particle's vertical speed in water is shown for one-way and two-way coupling and for a reference fluid with parameters corresponding to water. The SPH-DEM results reproduce the analytical velocity curve within 0.3–1% error besides short-lived higher deviations at the initial onset of motion (approx 5%). One of the key assumptions of the SPH-DEM method (and any fluid-particle method that uses an unresolved fluid phase) is that the fluid resolution is sufficiently greater than the DEM particle diameter d. This ensures a smooth porosity field calculated via Eq. (6). By varying the fluid resolution h, we have found that accurate results are achieved as long as $h \geq 2d$.

3.3 Validation case 2: Sedimentation of a Constant Porosity Block

The second test case (CPB) follows the sedimentation of a rigid porous block made up of a regular grid of DEM particles that cannot move relative to each other [10]. The porosity ϵ of the block determines the particle separation. As the block falls, the fluid is displaced and flows upward through the block, affecting the terminal velocity. All these simulations use the Di Felice drag law, which is one possibility to incorporate the effects of neighbouring particles on the drag force.

Varying the porosity of the CPB allows us to evaluate the accuracy of the SPH-DEM model at different porosities. Figure 3(right) shows the scaled terminal velocity of the CPB over a range of porosities from $\epsilon = 0.6$ to 1.0. The results for two different fluid resolutions are shown, $h/d = 2$ and 6. The lower resolution leads to a systematically increased terminal velocity due to a reduced drag at the edges of the block, caused by an excessive smoothing of the porosity discontinuity by the large width of the smoothing kernel, a feature not restricted to SPH-DEM but common to

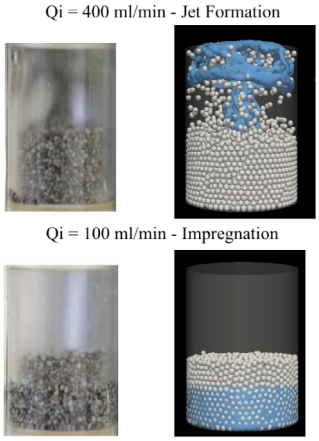

Fig. 4. Dispersion of a dry granular bed of poppy seeds by a 1 mm central injection hole. Left: experimental dispersion patterns shortly after liquid injection starts. Right: pseudo-Three-Phase SPH-DEM simulations. Grains are represented using white spheres and the liquid free-surface is colored in blue. Top row: a 400 ml/min inlet flow rate generates a jet. Bottom row: a slower 100 ml/min flow rate induces a bottom-up impregnation [41].

any fluid-particle method that uses an unresolved fluid phase. However, reducing the fluid resolution to $h/d = 2$ gives results better than 5% deviation (for the smallest ε) over the range of porosities tested. More details and other fluids, as well as other resolutions are discussed in Ref. [18], where also another test-case, the Rayleigh Taylor Instability (RTI) is introduced and used to study moving particles in the inverse settling set-up and the growth of the associated instability. Instead of continuing this, in the next subsection, we show one example with free boundaries, where the SPH-DEM method is at its best.

3.4 Dispersion example: Effect of inlet flow rate

Reference [41] compares experiments and SPH-DEM simulations of the dispersion of poppy seeds contained in a cylindrical cell, by liquid injected from a 1 mm diameter inlet at the bottom of the cell. The cell diameter is $d_{\text{cell}} = 23$ mm and the cell height $h_{\text{cell}} = 30$ mm. The outlet occupies all the top surface of the cell and is permeable to the liquid, but not to the grains. The grain density is $\rho_p = 1160$ kg/m^3 and their average diameter is $d = 1.1$ mm. The total mass of grains in the cell is 4.0 g, which corresponds to a bed height of about 14 mm.

The cylindrical cell and the cylindrical inlet/outlet are modelled as no-slip boundaries in the SPH-DEM simulation, using a single layer of SPH repulsive force particles [77]. The presence of the top filter is captured by including a top horizontal wall permeable to the fluid, but not to the grains. The DEM grains are allowed to settle into a packed arrangement before the inlet jet is turned on at $t = 0$. At this point SPH particles are added to the lower inlet with a constant velocity and rate that matches the experimental inlet flow rate Q_i. The air is assumed to have no influence on the results and is modelled implicitly by the absence of SPH fluid particles.

In Ref. [41], a range of inlet flow rates $50 \leq Q_i \leq 600$ ml/min was simulated. The behavior changes with increasing in-flow intensity. And the behavior predicted by simulations closely matches that of the experimental results, including the cut-off point at $Q_i = 100$ ml/min. Below this cut-off point the jet failed to fluidize the bed

and the dispersion cell filled with fluid from the bottom up to the outlet height. The movement of DEM grains was minimal until the bed had been completely immersed, which qualitatively matches the experimental results. Figure 4 shows snapshots from the simulations. Grains are represented using white spheres and the water free-surface is colored in blue. For $Q_i = 100\,\mathrm{ml/min}$ the grains do not move significantly and the fluid free-surface height linearly grows over time from the bottom to the top of the cell. The fluid free-surface is approximately constant over the horizontal width of the cell. For $Q_i = 400\,\mathrm{ml/min}$ the jet quickly breaks through the center of the grain bed, dispersing a large number of grains throughout the cell. The jet is so strong that it impacts on the top of the cell, whereas for smaller Q_i the jet did not reach the top. Once the jet breaks through, the cell fills with fluid from top to bottom until the DEM grains are fully immersed.

4 Conclusion

We have summarized the advantages and disadvantages of a number of simulation algorithms for particle-laden flows. Two recent state of the art implementations based on a DEM algorithm for the particles coupled to a multicomponent LBM or an SPH implementation for the involved solvents were presented and some specific applications were highlighted. To conclude, there is no perfect candidate on the market, but the method of choice has to be carefully selected depending on the physical problem. Of particular importance are the relevance of long-range hydrodynamic interactions, particle concentration and shape, the ratio of Brownian and advective forces, the role of inertia, or non-hydrodynamic particle–particle interactions such as electrostatic or van der Waals forces.

References

1. M.M. Dupin, I. Halliday, C.M. Care, L. Alboul, L.L. Munn, Phys. Rev. E **75**, 066707 (2007)
2. C. Aidun, J. Clausen, Annu. Rev. Fluid Mech. **42**, 439 (2010)
3. T. Krüger, F. Varnik, D. Raabe, Comput. Math. Appl. **61**, 3485 (2011)
4. F. Janoschek, F. Toschi, J. Harting, Phys. Rev. E **82**, 056710 (2010)
5. H.L. Goldsmith, R. Skalak, Annu. Rev. Fluid Mech. **7**, 213 (1975)
6. A. Leonardi, F. Wittel, M. Mendoza, H. Herrmann, Multiphase debris flow simulations with the discrete element method coupled with a lattice-Boltzmann fluid. In *Proceedings of III International Conference on Particle-based Methods, PARTICLES 2013* (2013)
7. G. Sauermann, A. Poliakov, P. Rognon, H. Herrmann, Geomorphology **36**, 47 (2000)
8. A. Araújo, E. Partelli, T. Pöschel, J. Andrade Jr., H. Herrmann, Sci. Rep. **3**, 2858 (2013)
9. A. Lorke, M. Winterer, R. Schmechel, C. Schulz, *Nanoparticles from the Gas Phase – Formation, Structure, Properties* (Springer, Berlin, 2012)
10. M.R. Robinson, S. Luding, M. Ramioli, Grain sedimentation with SPH-DEM and its validation. In *Powders and Grains 2013 – AIP Conf. Proc.*, Vol. 1542 (2013), p. 1079
11. Y. Tsuji, T. Oshima, Y. Morikawa, KONA **3**, 38 (1985)
12. T. Tanaka, T. Kawaguchi, Y. Tsuji, Int. J. Modern Phys. B **7**, 1889 (1993)
13. W. Kalthoff, S. Schwarzer, G. Ristow, H. Herrmann, Int. J. Mod. Phys. C **7**, 543 (1996)
14. K. Chu, A. Yu, Powder Technol. **179**, 104 (2008)
15. J. Link, L. Cuypers, N. Deen, J. Kuipers, Chem. Eng. Sci. **60**, 3425 (2005)
16. N. Deen, M.V.S. Annaland, M.V.D. Hoef, J. Kuipers, Chem. Eng. Sci. **62**, 28 (2007)
17. M.V.D. Hoef, M.V.S. Annaland, N. Deen, J. Kuipers, Annu. Rev. Fluid Mech. **40**, 47 (2008)
18. M.R. Robinson, M. Ramioli, S. Luding, Int. J. Multiphase Flow **59**, 121 (2013)

19. S. Srivastava, K. Yazdchi, S. Luding, Phil. Trans. R. Soc. A **372**, 20130386 (2014)
20. A. Leonardi, F. Wittel, M. Mendoza, H. Herrmann, Comput. Part. Mech. **1**, 3 (2014)
21. W. Ge, L. Lu, J. Xu, Y. Yue, X. Liu, L. Li, EMMS-based discrete particle method (EMMS-DPM) for simulation of gas-solid flows (2014) under review
22. N. Guo, J. Zhao, Int. J. Numer. Meth. Engng. (2014) (in press) – DOI: 10.1002/nme.4702
23. M. Hütter, J. Colloid Int. Sci. **231**, 337 (2000)
24. D. Petera, M. Muthukumar, J. Chem. Phys. **111**, 7614 (1999)
25. P. Ahlrichs, R. Everaers, B. Dünweg, Phys. Rev. E **64**, 040501 (2001)
26. L.E. Silbert, J.R. Melrose, R.C. Ball, Phys. Rev. E **56**, 7067 (1997)
27. G. Bossis, J.F. Brady, J. Chem. Phys. **80**, 5141 (1984)
28. A. Sierou, J.F. Brady, J. Fluid Mech. **448**, 115 (2001)
29. T. Phung, J. Brady, G. Bossis, J. Fluid Mech. **313**, 181 (1996)
30. J.F. Brady, G. Bossis, Annu. Rev. Fluid Mech. **20**, 111 (1988)
31. M. Loewenberg, E. Hinch, J. Fluid. Mech. **321**, 395 (1996)
32. H.A. Knudsen, J.H. Werth, D.E. Wolf, Eur. Phys. J. E **27**, 161 (2008)
33. P. Español, P. Warren, Europhys. Lett. **30**, 191 (1995)
34. A. Ladd, R. Verberg, J. Stat. Phys. **104**, 1191 (2001)
35. A. Komnik, J. Harting, H. Herrmann, J. Stat. Mech: Theor. Exp., P12003 (2004)
36. G. Gompper, T. Ihle, D. Kroll, R. Winkler, *Multi-Particle Collision dynamics: A Particle-Based Mesoscale Simulation Approach to the Hydrodynamics of Complex Fluids* (Springer, 2009), p. 1
37. A. Malevanets, R. Kapral, J. Chem. Phys. **110**, 8605 (1999)
38. A. Malevanets, R. Kapral, J. Chem. Phys. **112**, 7260 (2000)
39. M. Hecht, J. Harting, T. Ihle, H. Herrmann, Phys. Rev. E **72**, 011408 (2005)
40. M. Hecht, J. Harting, M. Bier, J. Reinshagen, H. Herrmann, Phys. Rev. E **74**, 021403 (2006)
41. M.R. Robinson, S. Luding, M. Ramioli, SPH-DEM simulations of grain dispersion by liquid injection. In *Powders and Grains 2013 – AIP Conf. Proc.*, Vol. 1542 (2013), p. 1122
42. A. Fogelson, C. Peskin, J. Comput. Phys. **79**, 50 (1988)
43. S. Schwarzer, K. Höfler, B. Wachmann, Comp. Phys. Comm. **268**, 121 (1999)
44. K. Höfler, S. Schwarzer, Phys. Rev. E **61**, 7146 (2000)
45. F. Fonseca, H. Herrmann, Physica A **342**, 447 (2004)
46. F. Fonseca, H. Herrmann, Physica A **345**, 341 (2005)
47. S. McNamara, E. Flekkøy, K. Måløy, Phys. Rev. E **61**, 658 (2000)
48. M. Strauß, H. Herrmann, S. McNamara, G. Niederreiter, K. Sommer, Particle Technol. **162**, 16 (2006)
49. M. Strauß, S. McNamara, H. Herrmann, Granular Matter **9**, 35 (2007)
50. W. Ramsden, Proc. R. Soc. London **72**, 156 (1903)
51. S. Pickering, J. Chem. Soc., Trans. **91**, 2001 (1907)
52. S. Succi, *The Lattice Boltzmann Equation for Fluid Dynamics and Beyond* (Oxford University Press, Oxford, 2001)
53. X. Shan, H. Chen, Phys. Rev. E **47**, 1815 (1993)
54. X. Shan, H. Chen, Phys. Rev. E **49**, 2941 (1994)
55. M.R. Swift, E. Orlandini, W.R. Osborn, J.M. Yeomans, Phys. Rev. E **54**, 5041 (1996)
56. S. Lishchuk, C. Care, I. Halliday, Phys. Rev. E **67**, 036701 (2003)
57. J. Harting, H. Herrmann, E. Ben-Naim, Europhys. Lett. **83**, 30001 (2008)
58. K. Stratford, R. Adhikari, I. Pagonabarraga, J.-C. Desplat, M. Cates, Science **309**, 2198 (2005)
59. A. Joshi, Y. Sun, Phys. Rev. E **79**, 066703 (2009)
60. F. Jansen, J. Harting, Phys. Rev. E **83**, 046707 (2011)
61. S. Frijters, F. Günther, J. Harting, Soft Matter **8**, 6542 (2012)
62. F. Günther, F. Janoschek, S. Frijters, J. Harting, Comput. Fluids **80**, 184 (2013)
63. B. Binks, T. Horozov, *Colloidal Particles at Liquid Interfaces* (Cambridge University Press, 2006)

64. B. Binks, Cur. Opin. Colloid Interface Sci. **7**, 21 (2002)
65. E. Kim, K. Stratford, R. Adhikari, M. Cates, Langmuir **24**, 6549 (2008)
66. A. Joshi, Y. Sun, Phys. Rev. E **82**, 041401 (2010)
67. N.-Q. Nguyen, A. Ladd, Phys. Rev. E **66**, 046708 (2002)
68. F. Janoschek, J. Harting, F. Toschi (submitted) (2014)
69. G. Taylor, Proc. R. Soc. Lond. Ser. A **138**, 41 (1932)
70. G. Taylor, Proc. R. Soc. Lond. Ser. A **146**, 501 (1934)
71. B. Kaoui, J. Harting, C. Misbah, Phys. Rev. E **83**, 066319 (2011)
72. T. Anderson, R. Jackson, Ind. Eng. Chem. Fundam. **6**, 527 (1967)
73. J.J. Monaghan, Rep. Prog. Phys. **68**, 1703 (2005)
74. M. Robinson, J. Monaghan, Int. J. Num. Meth. Fluids **70**, 37 (2012)
75. D. Price, J. Comp. Phys. **231**, 759 (2012)
76. R. Di Felice, Int. J. Multiph. Flow **20**, 153 (1994)
77. J.J. Monaghan, J. Comp. Phys. **110**, 399 (1994)